Published by IOP Publishing for Sissa Medialab

Received: *November 21, 2024*
Accepted: *March 3, 2025*
Published: *March 27, 2025*

LHCb RICH Fast-timing photon detection at the SPS charged particle beam

M. Bartolini[a], **R. Bolzonella**[b,c], **F. Borgato**[d], **R. Cardinale**[e,f], **L.N. Cojocariu**[g], **A. Cotta Ramusino**[c], **V. Duk**[h], **L. Fantini**[h,i], **D. Foulds-Holt**[a], **F. Keizer**[j,*], **R. Malaguti**[c], **L. Malentacca**[j,k], **G. Martelli**[h,i], **S. Minutoli**[f], **S. Okamura**[b,c], **F. Oliva**[l], **R. Pestotnik**[m], **D. Piedigrossi**[j], **V.M. Placinta**[g], **A. Seljak**[m] and **S.A. Wotton**[a]

[a] *Cavendish Laboratory, University of Cambridge, Cambridge, United Kingdom*
[b] *Università di Ferrara, Ferrara, Italy*
[c] *INFN Sezione di Ferrara, Ferrara, Italy*
[d] *Università degli Studi di Padova and INFN Sezione di Padova, Padova, Italy*
[e] *Università di Genova, Genova, Italy*
[f] *INFN Sezione di Genova, Genova, Italy*
[g] *Horia Hulubei National Institute of Physics and Nuclear Engineering, Bucharest-Magurele, Romania*
[h] *INFN Sezione di Perugia, Perugia, Italy*
[i] *Università di Perugia, Perugia, Italy*
[j] *European Organization for Nuclear Research (CERN), Geneva, Switzerland*
[k] *Università di Milano-Bicocca, Milano, Italy*
[l] *School of Physics and Astronomy, University of Edinburgh, Edinburgh, United Kingdom*
[m] *Jozef Stefan Institute, Ljubljana, Slovenia*
E-mail: floris.keizer@cern.ch

Abstract: The use of a new optoelectronic readout chain with $O(100)$ ps time resolution is a major milestone in the development of RICH detectors for environments with a high number of particle interactions per bunch crossing, such as the High-Luminosity LHC. A prototype chain, based on MAPMT and SiPM photon sensors coupled to readout electronics integrating the FastIC ASIC and a TDC-in-FPGA, is presented. The FastIC is an 8-channel ASIC for analogue-to-digital conversion with 25 ps time resolution. This ASIC is the predecessor of the FastRICH ASIC for the LHCb RICH upgrades. The signals from the photon detectors are timestamped in a custom multi-channel TDC-in-FPGA designed using a multi-phase clock sampling architecture with an average bin width of 150 ps. The prototype optoelectronic readout chain was tested in a charged particle beam of 180 GeV/c hadrons at the CERN SPS facility. The reference time-of-arrival of the particle tracks was measured with about 100 ps time resolution and the number of tracks per event was registered using a particle tracking system. The single-photon time resolution of the MAPMT sensors is extracted using a binned method in order to correct for the calibrated TDC bin widths and detector time-walk. The resulting best estimate of $\sigma = 182 \pm 24$ ps is in agreement with pulsed-laser measurements in the lab and consistent with the expectations from the manufacturer.

Keywords: Front-end electronics for detector readout; Timing detectors; Cherenkov detectors; Detector alignment and calibration methods (lasers, sources, particle-beams)

*Corresponding author.

https://doi.org/10.1088/1748-0221/20/03/P03034

2025 JINST 20 P03034

Contents

1 Introduction

In a variety of high-energy physics experiments, particle identification (PID) is performed by ring-imaging Cherenkov (RICH) detectors, which generally consist of a Cherenkov radiator, optical system and single-photon detection. The use of sub-nanosecond timing information at the photon detector can improve the PID performance, especially at conditions of high track multiplicity and pile-up of events [1]. In this paper, a prototype optoelectronic chain with sub-nanosecond timing capabilities will be presented and its single-photon time resolution (SPTR) demonstrated at the charged particle beam facility of the CERN SPS.

The studies are performed in the context of the upgrades programme of the LHCb experiment at CERN, which performs searches for new physics through studies of CP-violation and decays of heavy-flavour hadrons. There are two RICH detectors in LHCb [2]. The RICH 1 detector is located upstream of the LHCb dipole magnet and performs charged hadron ID in the momentum range of

2025 JINST 20 P03034

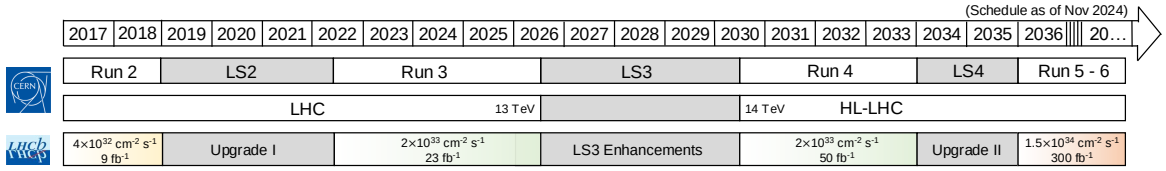

Figure 1. Timeline of the LHCb RICH upgrade programme at the (HL-)LHC.

2.6 to 60 GeV/c using C_4F_{10} as a gas radiator. The downstream RICH 2 detector operates between 15 and 100 GeV/c using CF_4 as a gas radiator. A timeline of the RICH upgrades programme is shown in figure 1. During LHC Run 3 and Run 4, multi-anode photomultiplier tubes (MAPMTs) are used for single-photon detection [2]. At Run 3, the MAPMT signals are shaped and discriminated by the CLARO front-end ASIC [3] and the digital signals processed using an FPGA, as shown in figure 2. Enhancements are foreseen for Run 4 (after LS3) where the front end electronics will be equipped with timing capabilities using a novel ASIC called the FastRICH [4–6]. The FastRICH will be capable of timestamping the photons using a 25 ps bin size. In addition, it will have advanced data-compression features and cover a wide input signal dynamic range. The use of picosecond-timing readout electronics is a major milestone and a novelty for the LHCb detector and large gaseous RICH detectors in general. For the LHCb Upgrade II, which foresees for a factor 7.5 increase in luminosity during Run 5, a full detector overhaul will be required [7]. The Run 4 electronics readout chain in figure 2 is designed to also be compatible with new sensor types for Run 5, although a significant increase in channel density would require a revision of the front-end layout.

In this paper, the first prototype optoelectronic chain with timing information and an expected resolution of $\sigma \approx 150$ ps to 200 ps for the LHCb RICH detector is presented. A new readout front-end ASIC, called the FastIC (Fast Integrated Circuit) [8], is introduced. The FastIC was developed by the University of Barcelona and CERN and precedes the FastRICH currently being designed. The FastIC, similar to the FastRICH, can be flexibly coupled to different sensor candidates for LHCb Upgrade II, owing to its wide input signal dynamic range. This prototype described in section 2 marks the start of a sequence of developments evolving towards a small-scale detector prototype of a future upgrade LHCb photon detector assembly. The development and understanding of the measurement techniques during the beam test campaign (sections 3 and 4) and the subsequent data analysis (sections 5 and 6)

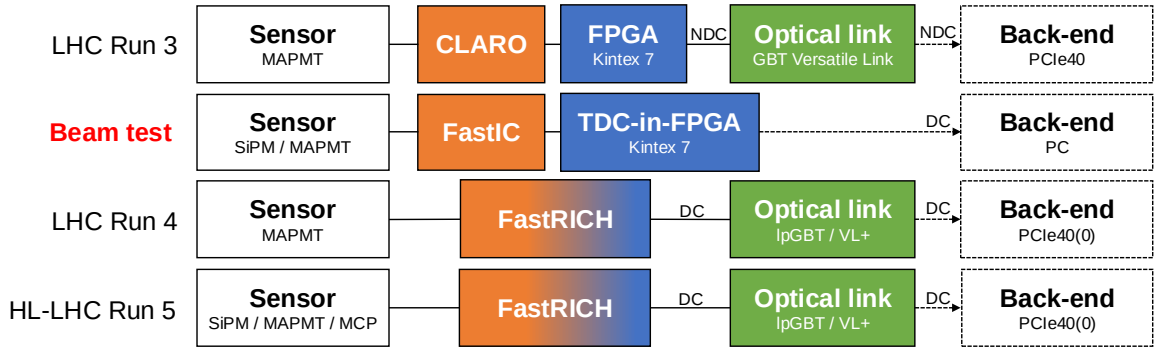

Figure 2. Schematic of the evolution of the LHCb RICH optoelectronic readout chain from the present Run 3 to the high-luminosity Run 5. A transition is made from no data compression (NDC) to data compression (DC).

2025 JINST 20 P03034

for sub-nanosecond timing Cherenkov photon measurements lay an important foundation for further research for the RICH detectors and wider picosecond-timing community.

The main focus in these studies lies in the analysis of the time-resolution of the 1-inch MAPMT, which constitutes the bulk of the photon detector plane that will be operated during Run 4 with picosecond-timing readout electronics. The successful operation and Cherenkov photon detection using the 2-inch MAPMT and SiPM sensors coupled to the new readout electronics sets an important precedence for future detailed timing studies and the hardware and operation is therefore described without its analysis of the time resolution.

2 Prototype fast-timing optoelectronic chain

A prototype optoelectronic chain with sub-nanosecond timing information was developed using the FastIC coupled to a time-to-digital converter (TDC) to provide photon timing information. The FastIC is operated in single-ended non-linear time-over-threshold (ToT) mode, where the length of the pulse at the comparator output retains the information of ToT, in a non-linear fashion. The FastIC is DC-coupled to an FPGA as shown in figure 3. An in-house TDC-in-FPGA was developed with nominal bin size of 150 ps [9] to capture the FastIC output. Here, the detection of the leading and trailing edge allows the ToT to be reconstructed in software. The FastIC readout chain was coupled to MAPMTs as well as SiPM arrays, which is one of the candidate photon sensors for LHCb Upgrade II.

2.1 FastIC and front-end board

The FastIC is an ASIC designed in 65 nm CMOS technology for the readout of precise timing detectors with intrinsic signal amplification. The 8-channel (single-ended) FastIC reads the signals delivered by a sensor and processes these in a current-mode method, the low-frequency input impedance being approximately 16 Ω. The precise-timing input stage sends each incoming signal to a fast current discriminator which compares the signal with a programmable threshold. The leading edge of the signal at the comparator output retains the signal time-of-arrival (ToA) information. In this mode of operation, the ToT is non-linear and the maximum rate is above 50 MHz, depending also on the details of the input

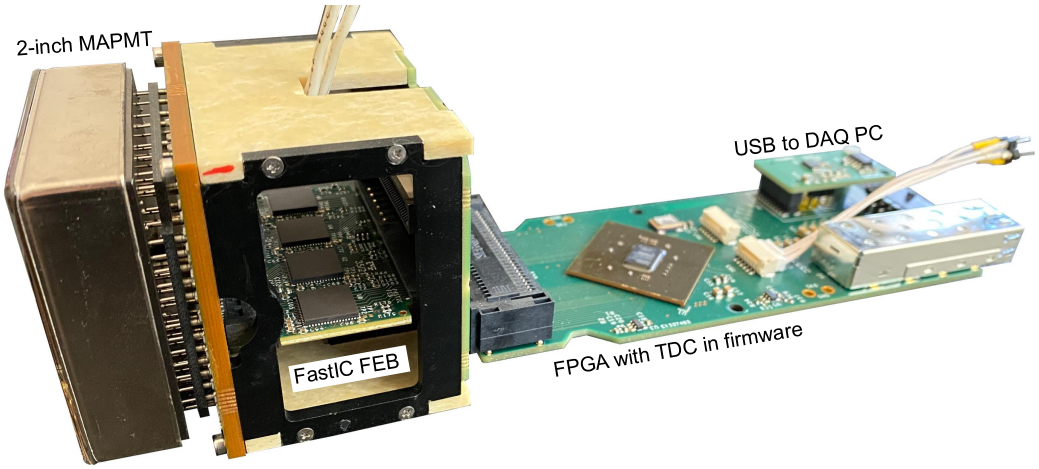

Figure 3. Prototype studied at the CERN SPS beam test with a 2-inch MAPMT coupled to the FastIC ASIC read out by a TDC-in-FPGA.

2025 JINST 20 P03034

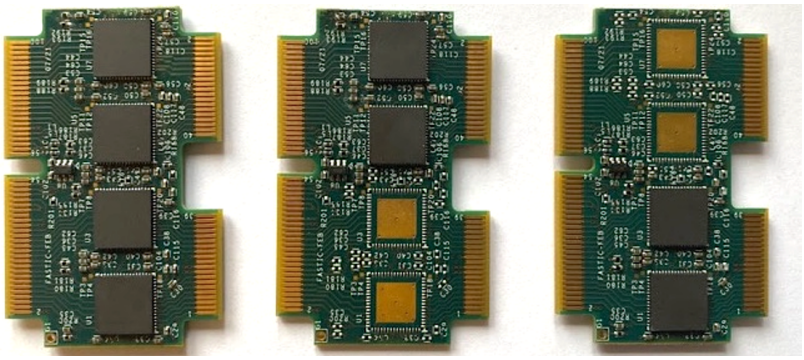

Figure 4. Front-end-boards with up to eight (four on each side of the board) FastICs mounted.

pulse shape. This ToT information allows an off-chip correction for the signal time-walk. The power consumption for the time output branch is approximately 6 mW per channel at 1.2 V. The input stage can be programmed to work in both positive or negative polarity and covers an input dynamic range of 5 µA to 20 mA. This provides important flexibility to couple the ASIC to different sensor types, such as MAPMTs with a negative input signal, or SiPMs with a positive signal and larger input capacitance.

The first available FastICs were successfully mounted on custom front-end boards (FEBs), which are shown in figure 4, and tested during the beam test campaign. Each FEB can host up to eight FastICs, four on each side. The PCB outline and edge connectors were designed to be compatible with the LHCb RICH Run 3 elementary cell (EC) design [2]. The FEB is optimised for short single-ended trace lengths to bring the analogue signal from the sensor to the FastIC inputs. From the FastIC output, the digital CMOS single-ended signals are routed from the FEB to the digital board with TDC-in-FPGA.

2.2 Digital readout board

The readout board serves to capture the digital signals from the FastIC ASICs and to format and transport the data to the data acquisition (DAQ) system. It also serves as a configuration and control interface for the front-end electronics. The shape and size of the board are designed to be compatible with instrumenting a close-packed array of ECs.

The board carries a Xilinx Kintex-7 XC7K70T676FFG-1C FPGA. 128 IO pins are routed to EC outputs through a Samtec connector. Additional IOs are routed through the same connector to the serial configuration interface (I2C) and reset pins of the front-end ASICs. The 1.2 V LVCMOS IO standard is used. Additional IO pins configured for the LVDS signalling standard are routed to connectors to receive a read-out trigger signal, external clock, and to provide a gate signal that can be used for flow control and synchronisation where multiple readout boards are in use. One of the available LVDS inputs can also be used to monitor an external reference signal or may be configured as an output to provide a trigger signal for the TDC calibration.

For this application, where only modest data rates of the order of 100 kHz are expected, the DAQ and controls hardware interfaces are provided through a USB2 interface to a DAQ PC. The board also implements an SFP interface connected to an FPGA gigabit transceiver which may be used where higher data rates are required. A graphical user interface running on the DAQ PC provides the operator with a flexible configuration and run control environment capable of simultaneously controlling and reading out several read-out boards.

2025 JINST 20 P03034

2.3 TDC-in-FPGA

A custom multi-channel TDC-in-FPGA core was designed using a multi-phase clock sampling architecture and implemented in the Kintex-7 FPGA on the digital readout board. When compared to other TDC architectures, the multi-phase clock sampling architecture has the key advantage of a resource-efficient design with increased stability against PVT (process, voltage and temperature) fluctuations [9]. This TDC design relies on 16 sampling Flip-Flops (FFs) to capture the input hit signal, with each of them clocked individually by eight phase-shifted copies of a 420 MHz clock. The clocks are phase-shifted by 22.5° providing a theoretical TDC bin width close to 148.8 ps.

2.3.1 Implementation

The clock network architecture was carefully designed to meet the timing requirements of this TDC-core. The simplified clocking architecture is depicted in figure 5. An external 80 MHz clock is used to drive three phase-locked loops (PLLs) to generate the clocks for the TDC core and for its readout logic. Eight copies of a 420 MHz clock are generated from the PLLs with a 22.5° phase shift within a phase range of 0° to 157.5°. These are used to clock the first eight sampling FFs on the rising edge. The remaining 8 sampling FFs are clocked on the falling edge to cover the entire 360° phase shift range.

The sampling logic was adopted from the work described in [10] and is based on 16 sampling FFs manually placed and routed within the FPGA. The input signal path was split in branches from the FPGA input pin to the input of every sampling FF. In this way, the input hit signal has the same delay path to all sampling FFs. Since each sampling FF captures the input signal with a nominal offset of about 150 ps, the pattern of 16 bits stored by the TDC core encodes the digital input signal, in particular the leading edge, corresponding to the ToA, and the trailing edge, from which the ToT can be calculated in software as the time difference between the leading and trailing edge. By constraining the sampling FFs to specific locations within the FPGA, the routing of the input signal branches through the FPGA switch boxes is fixed and independent of the synthesis run (figure 6). Careful placement of the FFs is required in order to equalise the routing delays from the input pin to the 16 sampling FFs. The residual variation of these delays results in variations in the TDC bin widths which must be calibrated and corrected in the data. Figure 7 shows the basic architecture of the TDC

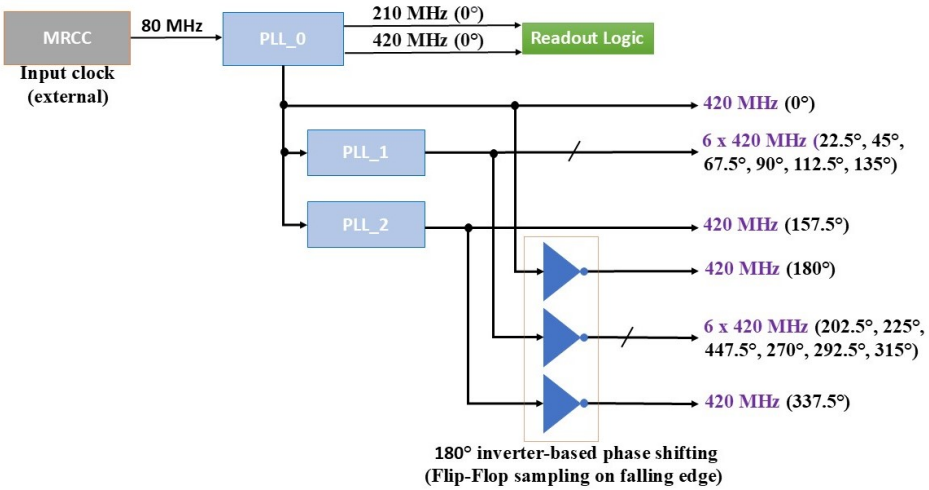

Figure 5. Simplified TDC clock distribution network.

2025 JINST 20 P03034

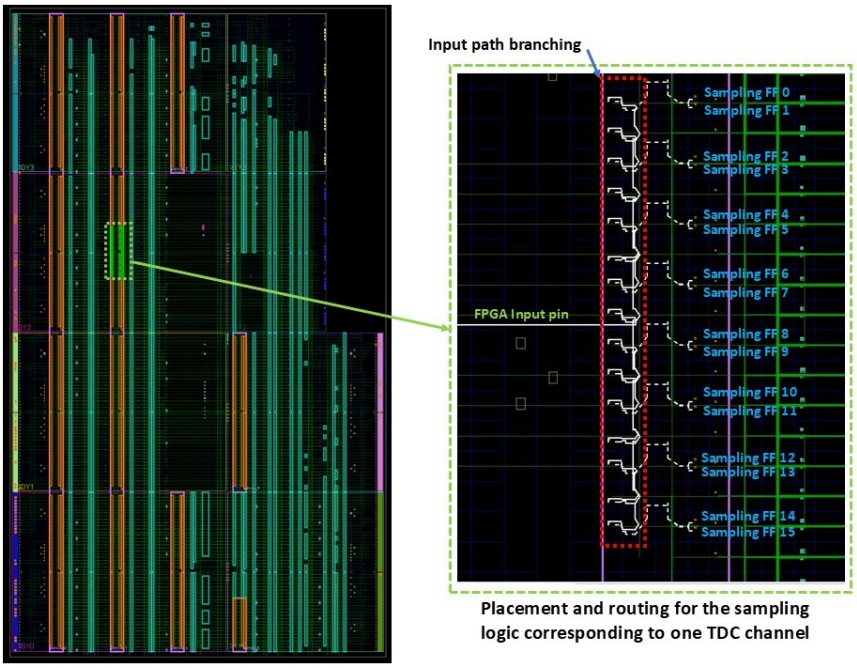

Figure 6. Physical placement of the TDC-core logic for multi-channel configuration within the Kintex-7 FPGA. On the left side, the physically constrained logic for all TDC channels is highlighted in orange and the TDC logic for one channel in green. The right side shows the TDC-core layout magnified.

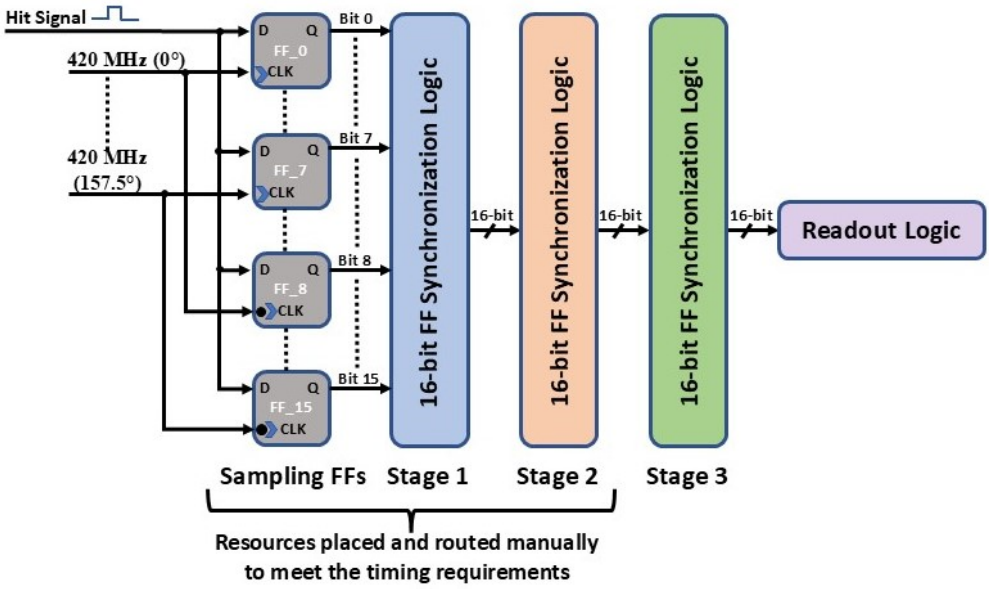

Figure 7. Basic architecture of the TDC-in-FPGA logic.

core logic. The sampled pattern is synchronised to a common clock domain through three FF-based synchronisation stages before filling the readout buffers.

The available resources of the Kintex-7 FPGA are sufficient to implement 34-channels and is the limiting factor in the number of front-end channels that may be instrumented in this application.

2025 JINST 20 P03034

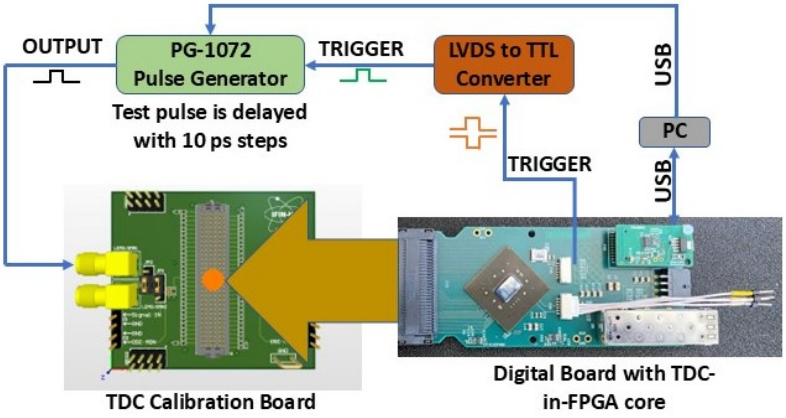

Figure 8. Schematic of the calibration setup, where the TDC calibration board is used to fanout the FPGA IOs to the reference pulse generator.

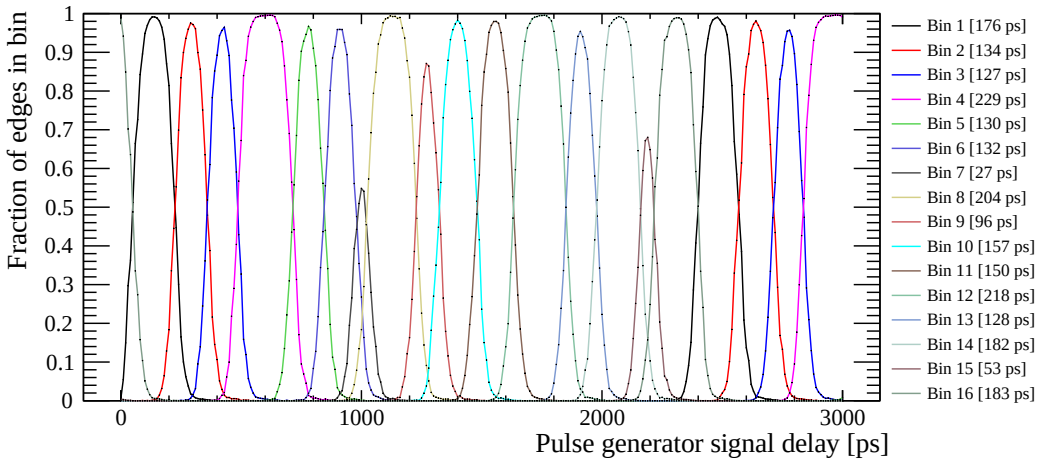

Figure 9. Single-channel data from a TDC calibration run. The fraction of detected pulses is shown as a function of the delay setting of the pulse generator signal, for each of the 16 bins which are repeated at the 420 MHz TDC clock frequency.

2.3.2 Calibration

Calibration of the TDC core was performed using a programmable pulse generator[1] triggered by a signal generated in the FPGA. Once triggered, the pulse generator injects a 1.0 V pulse into the TDC channel inputs through the fan-out card shown in figure 8. The pulse has configurable delay, allowing a control sequence to be implemented to sweep through the TDC window in steps of 10 ps. 2048 samples were recorded at each step.

Signal loading by the PCB traces and FPGA inputs causes the slew rate of the input signal to be reduced. Therefore, only two channels were connected per calibration run. The different PCB mapping for different sensor types (1-inch MAPMT, 2-inch MAPMT and SiPM) resulted in a different set of FPGA IOs used for each of these digital readout chains. The firmware was resynthesised for these options, and the calibration repeated on each chain. Figure 9 shows the fraction of pulses

[1]Active Technologies Pulse Rider PG-1072.

2025 JINST 20 P03034

arriving in a specific bin against the pulse delay for a typical channel. The bin width is defined as the range over which a leading edge is detected for more than 50% of the generated triggers. For bins that at no point detect over 50% of the generated triggers, the width is defined as the gap between the 50% limits of the two neighbouring bins. The recorded calibration files are used in the analyses in section 5 to convert from TDC bin number to time.

2.4 Single-photon sensors

MAPMT and SiPM photon sensors were used during the beam test campaign. Figure 10 shows the MAPMT ECs on the left-hand side and the SiPM EC on the right-hand side, with the nominal Cherenkov-ring position indicated by the orange dotted-line.

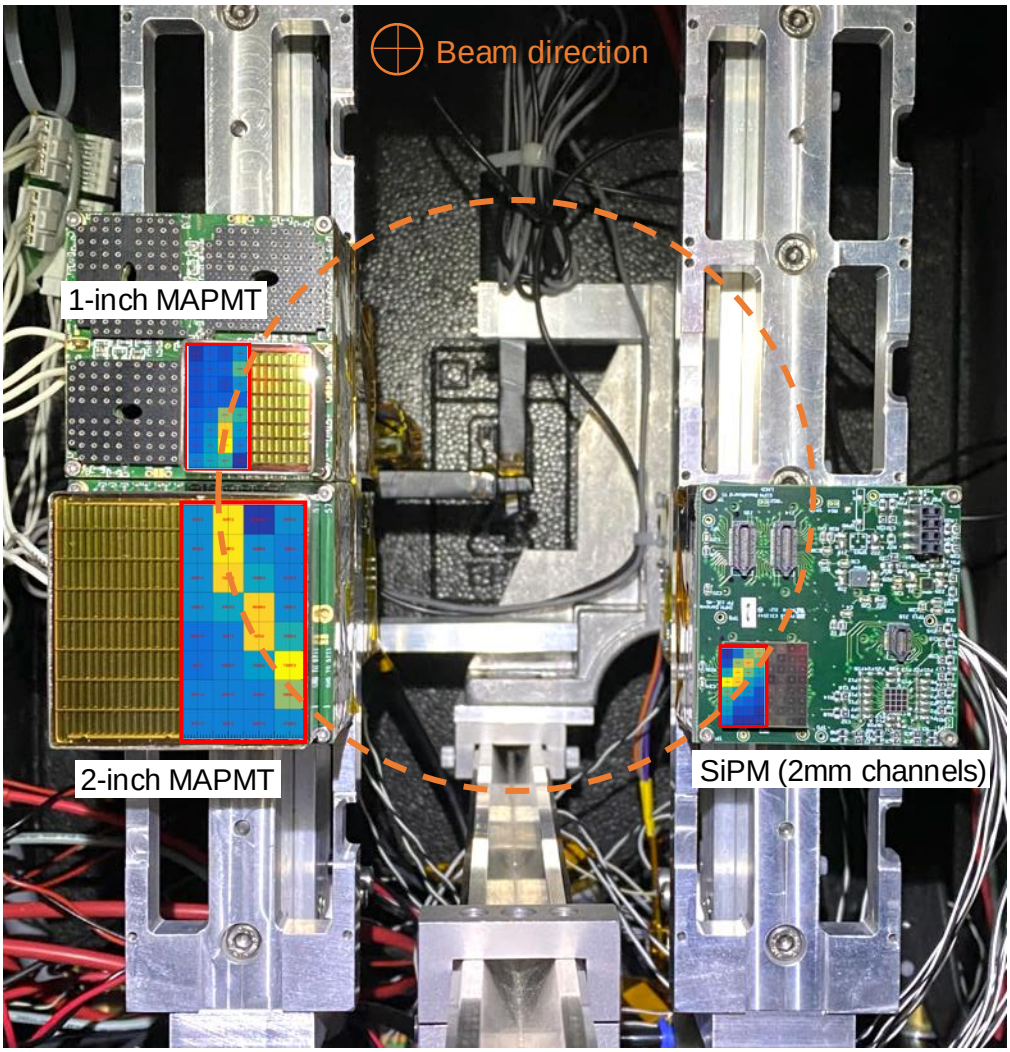

Figure 10. Image of part of the beam test setup viewed from the beam direction. The orange-dotted line represents the position of the Cherenkov photon ring and the integrated hit maps are overlaid on the MAPMT and SiPM sensors. In this image a crossed scintillator pair is mounted at the position of the MCP-PMT in order to align the system with the charged particle beam before data taking.

2025 JINST 20 P03034

2.4.1 Multianode photomultiplier tubes (MAPMTs)

The LHCb RICH Run 3 detector uses two types of Hamamatsu MAPMTs[2] with 8×8 pixels: the 1-inch R13742, custom version of the R11265 model [11], and the 2-inch R13743, custom version of the R12699 [12]. The 1-inch MAPMT contains 12 dynodes with nominal signal transit time of 5.1 ns and nominal transit-time spread (TTS) of approximately 150 ps. The 2-inch MAPMT has 10 dynodes resulting in 5.3 ns transit time and about 120 ps TTS. The MAPMTs are mounted on a PCB with custom sockets, called the BaseBoard (BB), which provides the bias voltage of around -1000 V to the photo-cathode and the dynodes through a resistor-divider chain. Additionally, it connects the MAPMT anodes to the FEBs [2].

2.4.2 Pulsed-laser measurements of the MAPMT TTS

In order to investigate its analogue signal shape and time resolution prior to the coupling to the new readout chain, the 1-inch MAPMT was tested in the laboratory using a picosecond pulsed laser. The laser[3] emits 50 ps FWHM pulses, which are interpreted to have a Gaussian profile with $\sigma \approx 21$ ps, at a wavelength of 405 nm using a monomode optical fibre. Photon absorption filters are used to ensure single-photon illumination. A mask covered the MAPMT cathode except for a 2 mm^2 aperture to illuminate a channel of interest, avoiding cross-talk from signals in neighbouring channels. The single-photon signal of the illuminated channel was sent to an oscilloscope[4] to measure the jitter as ΔToA with respect to the pulsed-laser synchronous output signal. The transit-time distribution in figure 11 was obtained by first fitting the recorded MAPMT signal shape with a crystal ball function, thereby removing any high-frequency noise components. The ΔToA is obtained using, in software, a constant-fraction discrimination (CFD) of 10 % of the MAPMT signal amplitude. At -1000 V bias voltage, a TTS of $\sigma = 145 \pm 5$ ps is obtained, which is compatible with the nominal value and serves as a reference value for the TTS obtained using the electronic readout chain.

2.4.3 SiPM and novel BaseBoard

SiPMs represent a promising candidate for the LHCb Upgrade II owing to their photon-detection efficiency, time resolution, gain comparable to that of a MAPMT, insensitivity to magnetic fields, low-bias operating voltage and limited cost. However, the sensors also suffer from high dark-count rates at room temperature, especially after exposure to radiation. During the beam test campaign, two different Hamamatsu SiPM arrays with 8×8 channels were introduced:

- S13361-2050AE-08 with 2.0 mm channel dimensions and 50µm cell pitch. At the suggested operating voltage of 54.1 V, the nominal gain is 1.7×10^6 with 0.08 µA dark current per channel and a dark-count rate of 300 kHz specified by the manufacturer.
- S14161-3050HS-08 with 3.0 mm channel dimensions and 50µm cell pitch. At the suggested operating voltage of 40.7 V the nominal gain is 2.5×10^6 with 0.6 µA dark current per channel (corresponding to about 1.5 MHz dark-count rate).

Two different BB versions for SiPMs, called BBv1 and BBv2, have been designed and produced [13]. The BBv1 shown in figure 10 connects to the S13361-2050AE-08 array through high

[2]Serial numbers FB1502 and FB2116 for the 1-inch model and FA0890 for the 2-inch model.
[3]Taiko LDH-IB-405-B Picosecond Diode Laser.
[4]DSA91204 Agilent Infiniium scope with Agilent 1169A active probe with N5426A solder-in ZIF tip.

2025 JINST 20 P03034

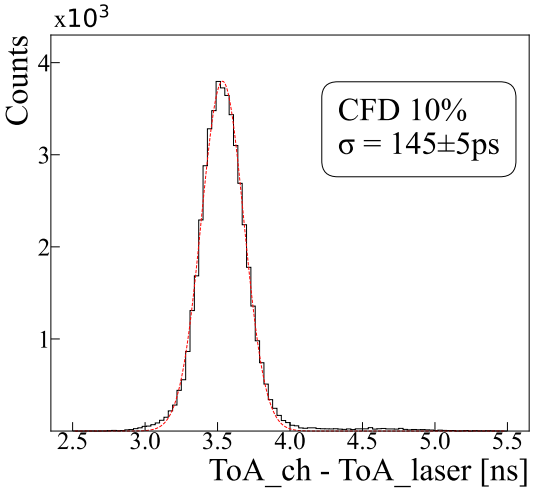

Figure 11. Transit-time distribution of a 1-inch MAPMT channel with respect to the pulsed-laser reference.

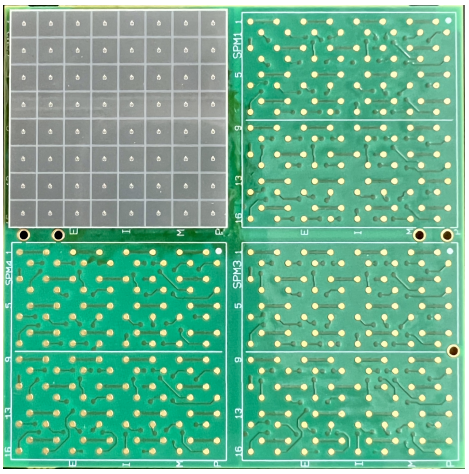

Figure 12. SiPM BBv2 with one out of four 8×8 SiPM arrays mounted.

density connectors for flexibility and modularity. The BB accommodates a variety of SiPM types for test purposes. The BBv2 shown in figure 12 hosts up to four S13361-2050AE-08 arrays in an arrangement with optimised geometrical fill factor. The LGA (Land-Grid Array) SiPMs are soldered directly onto the BBv2 for shortest signal paths to the FastIC inputs. The signal is read from the SiPM anodes with a common cathode. At the rear-side of the SiPM BBs, edge connectors are mounted to connect to up to four FEBs.

3 Experimental setup

The CERN SPS beam facility provides a charged hadron beam, primarily consisting of pions and protons, with a momentum of 180 GeV/c. The optics is placed on the beam line and the optoelectronic chain is read out in response to a trigger signal from the trigger-logic unit when a beam particle passes through the setup. The particle tracking system was used to add tracking information to the RICH data set. A pulsed-laser setup in the laboratory provided performance reference measurements of the optoelectronic readout chain.

3.1 Optical Cherenkov system and alignment

The sub-nanosecond time resolution and single-photon sensitivity of the readout chain was studied using Cherenkov photons generated by beam particles. In this way, the system can be demonstrated to operate under conditions that mimic the final experimental application, using realistic track reference timestamps and photon signals. These photons are emitted in and focused by a borosilicate lens,[5] in a similar arrangement to previous beam tests [14] and as seen at the top of figure 14. Figure 10 shows an image of the setup, inside its light-tight enclosure, from the direction of the beam passing through the centre. The Cherenkov ring generated by the beam passing through the lens (not mounted in the photograph) is illustrated by the orange-dotted line. Half of the channels of the 1-inch, 2-inch MAPMT

[5]Edmund Optics PCX condenser lens no.27509 with 150 mm diameter and 300 mm focal length.

2025 JINST 20 P03034

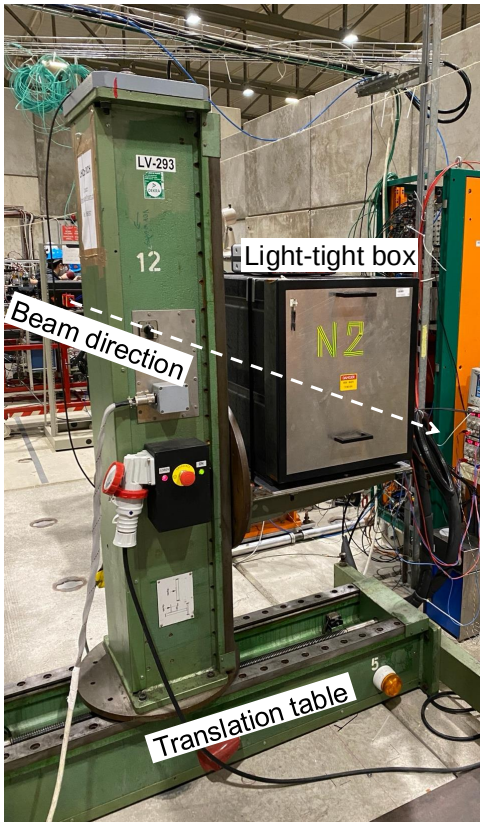

Figure 13. Image of the light-tight box mounted on the remotely-operated translation table for alignment with the charged particle beam.

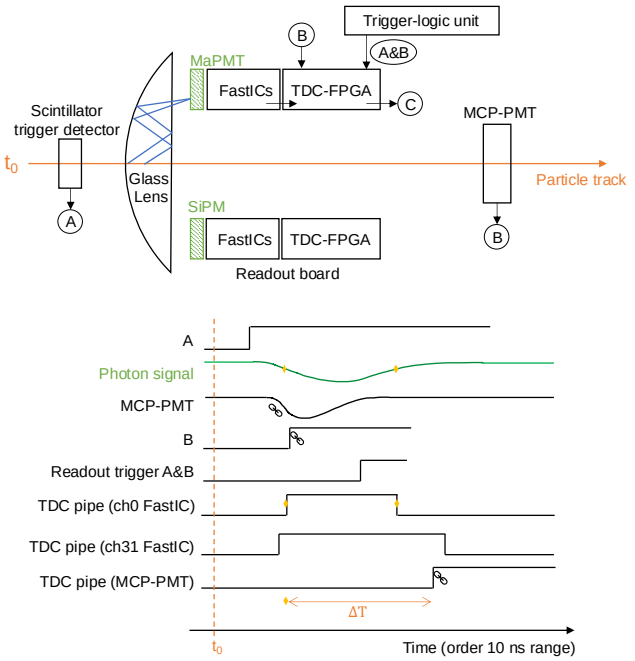

Figure 14. Schematic of the test beam setup. The MCP-PMT signal has a jitter of about 100 ps to the track time. ΔT is measured between the MCP-PMT and the photon signals from the FastIC using the TDC-in-FPGA. This simplified logic timing diagram does not represent the true signal delays and jitters.

and SiPM array are read out by the sub-nanosecond timing chain and the hit maps, recorded using beam data and integrated over time, are superimposed on the image to show the Cherenkov photon arcs.

In order to align the setup with the beam, two pairs of crossed scintillator detectors with $5 \times 5\,\mathrm{mm}^2$ area perpendicular to the beam were installed, one upstream of the lens and one downstream at a distance of 50 cm. The setup was positioned on a translation table to provide movement in the plane perpendicular to the beam, as shown in figure 13. The position was adjusted until the upstream and downstream scintillator detectors registered a maximum number of counts corresponding to the centre of the beam. The difference between the upstream and downstream position at the maxima was used to obtain the angle of the beam with respect to the setup, which was below 1 mrad. After alignment, the downstream scintillator detectors were replaced by a micro-channel plate photomultiplier tube (MCP-PMT)[6] in order to provide the track reference timestamp as described in the following sections.

3.2 Trigger and data acquisition (DAQ)

An FPGA-based trigger-logic unit is used to make the coincidence between the trigger sources and distribute the digital readout trigger to the optoelectronic chains. A schematic of the trigger operation in order to record the time difference, ΔT, between the Cherenkov photon signals and the track reference time is shown in figure 14.

[6] Burle 85001.

2025 JINST 20 P03034

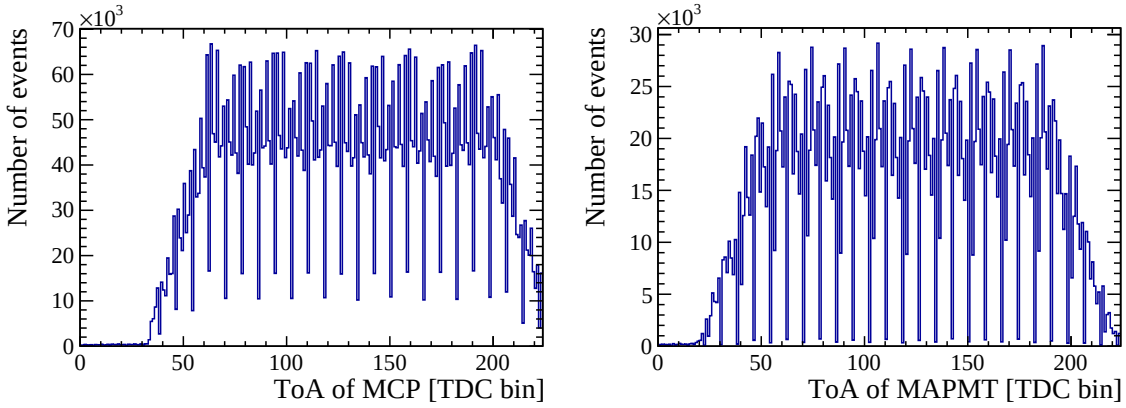

Figure 15. Left: recorded ToA distribution of the MCP-PMT with respect to the start of the TDC readout window. Right: recorded ToA distribution of a typical MAPMT channel with respect to the start of the TDC readout window.

At t_0 an asynchronous charged particle from the beam passes through the trigger system consisting of a crossed-finger scintillator detector (labelled *A* in the figure) and an MCP-PMT (*B*). The beam generates Cherenkov photons in the entrance window of the MCP-PMT which are collected at the photocathode. One of the four 1-inch MCP-PMT channels was centred on the particle beam and read out to provide the particle reference time for the system. The MCP-PMT signal is amplified by a custom circuit and discriminated using a CFD module.[7] The coincidence (*A&B*) performed by the trigger-logic unit is used as the synchronous readout trigger distributed to the readout boards and marks the start of the TDC readout window. Additionally, signal (*B*) from the MCP-PMT CFD output is sent to a dedicated channel (called *TDC pipe (MCP-PMT)* in the figure) in the TDC-in-FPGA in each readout board. The Cherenkov photons generated by the beam particle in the lens are detected by the MAPMT or SiPM sensors and the signals shaped and discriminated in the FastIC. Each readout board is coupled to 32 output channels from 4 FastICs and stores the digital signal traces (*TDC pipe (chX FastIC)* in the figure) over a 32 ns TDC readout window with 150 ps bins. The trigger logic is synchronous to the 40 MHz system clock while the beam is asynchronous. As a result the ToA of the photon signals are randomly distributed with one clock cycle (25 ns, or 168 TDC bins) as can be seen in figure 15. However, the signals from the optoelectronic chain and the MCP-PMT reference timestamp originate from the same track events and can therefore be paired for the analyses in section 5.

3.3 Track telescope and readout synchronisation

The SPS beam was recorded by a track telescope positioned approximately 2 metres upstream from the LHCb RICH setup. The telescope contains eight planes of silicon pixel detectors read out by the TimePix4 ASICs [15]. Each plane has a total active area around $24.6 \times 28.2\,\mathrm{mm}^2$ divided in square pixels of 55 µm pitch. The telescope data taking is continuous: when a run is started all hits are acquired and for each hit a timestamp is recorded. During offline analysis, the tracks are reconstructed from hits in each plane that have consistent times. External time reference signals can also be recorded by the tracking system through either a channel in the TimePix4 TDC or through

[7] CAEN N605 NIM module.

2025 JINST 20 P03034

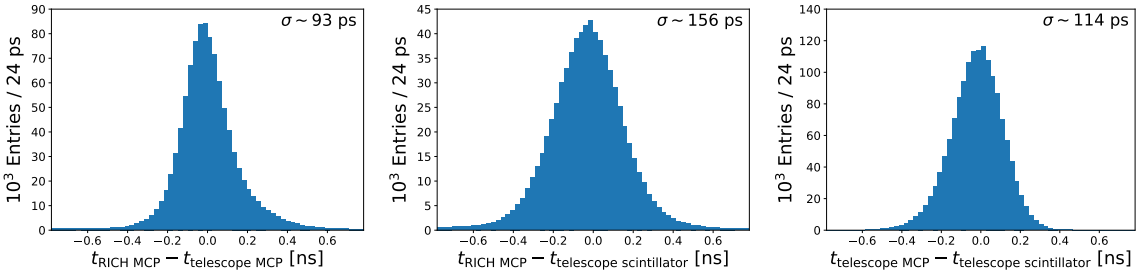

Figure 16. Left: distribution of the time difference between the RICH MCP-PMT and the telescope MCP-PMT. Centre: distribution of the time difference between the MCP-PMT and the telescope scintillator. Right: distribution of the time difference between the telescope MCP-PMT and the telescope scintillator.

a synchronised telescope picoTDC ASIC running in parallel [16]. This time reference is analysed to select tracks within a user-defined time interval around the timestamp.

The information about the number of tracks passing in the telescope is useful to identify events in the RICH setup with multiple particles and to estimate the expected number of hits per event in the MAPMTs. To synchronise the RICH system with the telescope, during dedicated combined runs the readout trigger from the RICH trigger-logic unit, also referred to as the RICH coincidence signal, and the CFD output signal of the RICH MCP-PMT are sent to the telescope picoTDC. This RICH MCP-PMT, which is the MCP-PMT in the RICH light-tight box and described in figure 14, is different from the telescope MCP-PMT, which was placed on the beam line inside the telescope setup to provide an additional and independent track timestamp.

Prior to the beam test, the RICH MCP-PMT resolution was measured in the laboratory using a pulsed-laser light source. A $\sigma_{\mathrm{MCP}}^{\mathrm{analogue}} \approx 47\,\mathrm{ps}$ resolution was obtained as the Gaussian standard deviation of the distribution of the difference between the MCP-PMT analogue signal ToA and the laser trigger time. This measurement was performed in the single-photon regime and observed to improve for multi-photon signals, which are expected to be generated by tracks through the MCP-PMT window. During the beam test, the combined runs with the telescope system could provide an estimate of the MCP-PMT track reference time resolution, now also including the CFD and readout electronics. The telescope external time reference is given by the telescope MCP-PMT and three crossed-finger scintillators. These signals are sent to the telescope picoTDC and their timestamps are recorded. The RICH MCP-PMT time resolution is obtained from the time difference between the RICH MCP-PMT and the telescope MCP-PMT ($\sigma_{t_{\mathrm{RICH,MCP}}-t_{\mathrm{tel,MCP}}}$, figure 16 left), the RICH MCP-PMT and the telescope scintillators ($\sigma_{t_{\mathrm{RICH,MCP}}-t_{\mathrm{tel,scint}}}$, figure 16 centre), the telescope MCP-PMT and the telescope scintillator ($\sigma_{t_{\mathrm{tel,MCP}}-t_{\mathrm{tel,scint}}}$, figure 16 right), by using the relation:

$$\sigma^2_{t_{\mathrm{RICH,MCP}}} = \frac{\sigma^2_{(t_{\mathrm{RICH,MCP}}-t_{\mathrm{tel,MCP}})} + \sigma^2_{(t_{\mathrm{RICH,MCP}}-t_{\mathrm{tel,scint}})} - \sigma^2_{(t_{\mathrm{tel,MCP}}-t_{\mathrm{tel,scint}})}}{2}. \tag{3.1}$$

Here, the Gaussian-equivalent standard deviations are extracted from the FWHM of the distributions in figure 16. The resulting time resolution of the RICH MCP-PMT is $\sigma_{t_{\mathrm{RICH,MCP}}} \approx 100\,\mathrm{ps}$, which is dominated by the CFD jitter.

2025 JINST 20 P03034

3.4 Beam parameters

The beam profile was measured for each particle spill using multi-wire proportional chambers, which were positioned in the experimental area a few metres downstream of the test setup. The Gaussian beam profile has a typical spread of $\sigma_x = 3.5$ mm and $\sigma_y = 4.8$ mm. The beam intensity is between 5×10^5 and 10^6 particles per spill.

The picoTDC of the telescope produces an absolute timestamp for each RICH coincidence signal and RICH MCP-PMT reference time. As shown in figure 17 (left), these follow the typical pattern of the consecutive spills of the SPS beam. Using the picoTDC timestamps, it is also possible to measure the rates of the MCP-PMT and RICH coincidence signals. Assuming that the particles arrive uniformly in time during a spill, the time difference between two consecutive coincidence signals, $dt[i] = t[i+1] - t[i]$, has an exponential distribution: $f(dt) = Ne^{-r \cdot dt}$ where r is the rate and N is the normalization factor. The rates obtained from the fit of the $dt[i]$ distribution by the exponential function are approximately 20 kHz for the RICH coincidence, shown in figure 17 (right), and 100 kHz for the MCP-PMT. This difference is mostly due to the relatively wide transverse beam dimensions and the smaller sensitive area of the RICH scintillator detectors than the MCP-PMT.

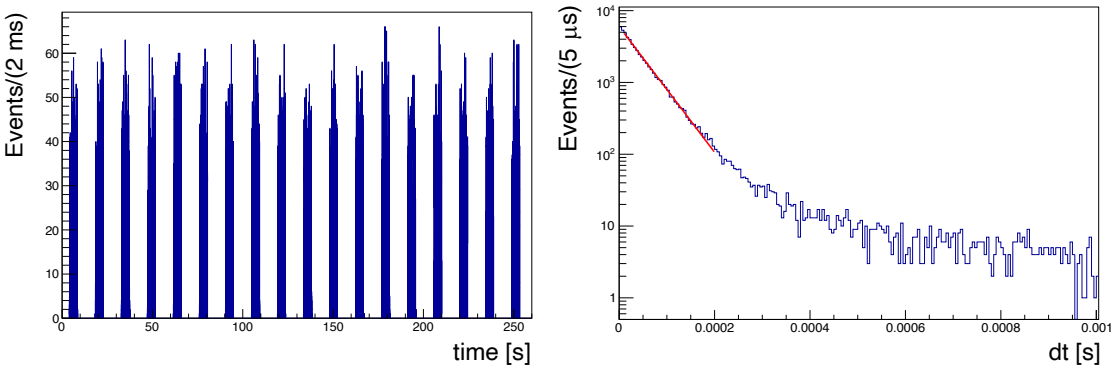

Figure 17. Left: RICH coincidence absolute time measured by the telescope picoTDC. Right: $dt[i]$ distribution for the RICH coincidence. For the definition of $dt[i]$, see text. The exponential fit is shown in red.

4 Photon detector working point

In this section, the strategy to find the threshold operating point for data-taking with the prototype optoelectronic chain is outlined. The operational aim is to study the timing, rather than to find the best photon detection efficiency. The stability, time resolution and relative photon detection efficiency at these working points are evaluated.

4.1 Threshold working point and FastIC stability

Channel-to-channel variations require tuning of the threshold for individual channels to maximise the signal-to-noise ratio. A threshold scan was performed on each channel, starting from a threshold above the baseline noise of the FastIC discriminator and therefore with a low digital output signal. The FastIC threshold was then reduced in 64 steps of 1.13 µA, recording a configurable number of 128 triggers at every step. These triggers are generated internally in the FPGA logic of the digital board and used to latch the FastIC output. While the photon sensor was connected and powered up during

2025 JINST 20 P03034

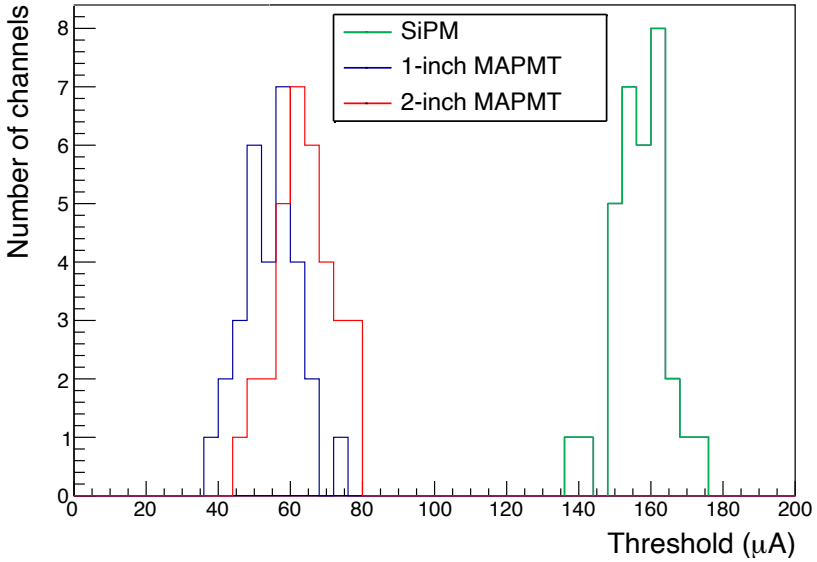

Figure 18. Distribution of the noise pedestals for the channels of the three different digital boards.

the threshold scans, this method of asynchronous triggering combined with the 32 ns readout window means that the threshold scans are performed in the absence of single-photon signals. The transition point between low and high FastIC output typically occurs within one 1.13 µA step. This transition point is taken as the noise pedestal and for all subsequent studies the threshold value for each channel will be set with respect to this noise pedestal of the channel. Figure 18 shows the distribution of the pedestals in the three digital boards. The added capacitance of the 3 mm SiPM channels increases the noise levels in the FastIC and resulted in a higher threshold value of the noise pedestal.

The prototype readout electronics were operated in single-ended output mode of the FastIC, with each channel routed through the backboard of the EC towards an FPGA input pin. The 1.2 V CMOS digital output drive strength needed to be set to its maximum value in order to be registered by the FPGA input. However, the combination of a high channel density and CMOS output could cause instabilities in the FastIC operation. Specifically, when the threshold was set close to the noise pedestal value, resulting in one or more channel outputs switching rapidly, a feedback mechanism was observed where the induced (digital) noise caused a cascade effect of more channels switching. This commonly led to the I2C communication being temporarily or permanently (until the next power-up of the ASIC) lost to the FastIC. In practice, the threshold scan to obtain figure 18 was therefore performed in an automated sequence for one channel at a time, while all other channels were set to the maximum threshold. During operation, the threshold value was set sufficiently above the pedestal to avoid the feedback mechanism. This operating point corresponded to 20.3 µA from the pedestal for the 1-inch MAPMT, 11.3 µA from the pedestal for the 2-inch MAPMT and 67.4 µA from the pedestal for the SiPM. In the next generation of the prototype optoelectronics chain, as well as in the future FastRICH ASICs, a differential output mode will be used, which is expected to mitigate the observed instability.

4.2 Pulsed-laser studies at varying threshold settings

A pulsed-laser setup was used at the CERN laboratory to record reference data sets to validate the MAPMT working points and time resolution using the full optoelectronic readout chain. Instead

2025 JINST 20 P03034

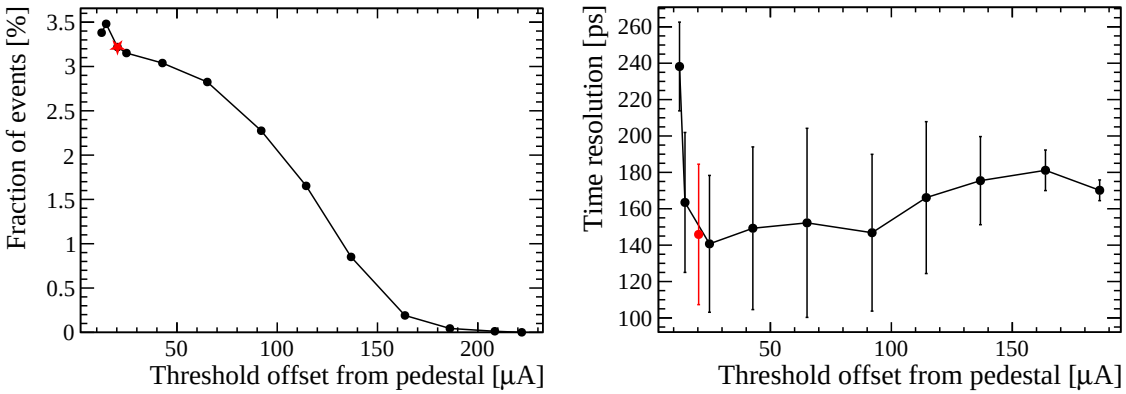

Figure 19. Left: fraction of events with a recorded hit in a single MAPMT channel as a function of the threshold offset. The red point represents the operational threshold during the beam test. Right: time resolution (sigma) as a function of the FastIC threshold offset from the pedestal. The red point represents the operational threshold during the beam test.

of the trigger-logic unit, the digital board is used to generate the laser trigger at 20 kHz rate. A copy of this trigger signal is stored in a TDC-in-FPGA channel to include the laser reference time in data. A diverging lens is used to illuminate most of the sensor surface at each trigger. The relative single-photon detection efficiency (PDE) and the SPTR were measured as a function of the threshold offset from the previously obtained noise pedestal. Figure 19 (left) shows the fraction of detected photons per laser trigger event, which is used as a measure of the relative PDE, for a typical 1-inch MAPMT channel. The data are recorded at a low laser intensity resulting in approximately 3 % of the events containing a photon. The relative PDE shows a broad S-curve due to the typical wide signal amplitude spectrum of the MAPMT. The time resolution of the channel is shown in figure 19 (right). This time resolution is obtained using the method described in section 5 and shows a good time resolution for a broad range of threshold settings. The data were recorded in the single-photon regime (at 3 % measured photon occupancy) with ten million events per step.

4.3 Bias voltage variations

The optoelectronic chain was studied at different MAPMT bias voltage settings, between −800 V and −1000 V in steps of 50 V. The threshold working point was fixed for all data sets. As shown in figure 20 (left), the ToT for two channels of the 1-inch MAPMT gets longer with increasing negative bias voltage due to the larger signal amplitudes. The ToT reported is the mean of a Gaussian fit to the ToT distribution. The offset in ToT between the channels depends in particular on channel-to-channel gain variations. The gain information from the manufacturer indicated an increase of about 30 % from the channel shown in red (low gain) to the channel in blue (high gain). The ΔToA distribution of a typical channel is shown in figure 20 (right): at fixed threshold, the ΔToA decreases with increasing negative bias voltage, due to the stronger signal amplification in the MAPMT and the application of a fixed discriminator threshold. The curves therefore represent the typical time-walk effect of earlier ToA for larger amplitude signals. Overall, these results demonstrate that the optoelectronic chain performs as expected and that the electronics is sensitive to small changes in ToA and ToT.

2025 JINST 20 P03034

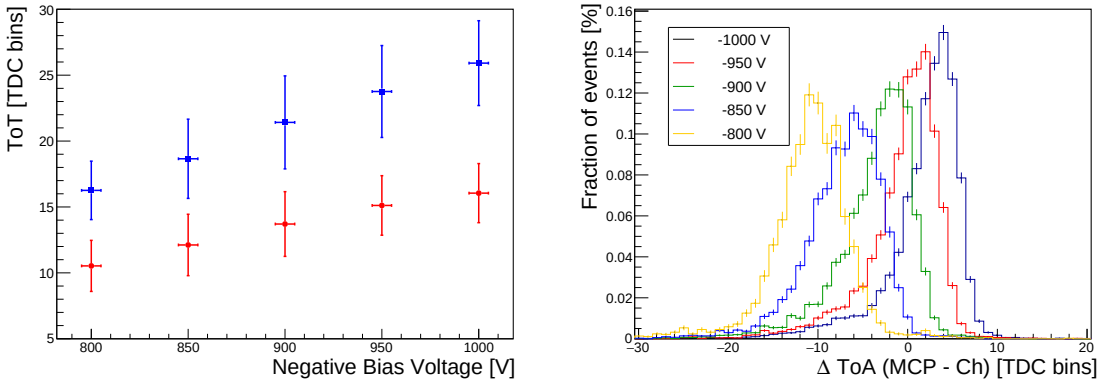

Figure 20. Left: time-over-threshold as a function of the bias voltage for two channels of the 1-inch MAPMT. A gain increase of 30 % from the channel in red to the channel in blue is specified by the manufacturer. Right: time-of-arrival distribution with respect to the MCP-PMT reference time for different MAPMT bias voltages at a fixed threshold working point.

5 Single-photon time resolution (SPTR)

In this section, the time resolution is presented for the 1-inch MAPMT, which covers two-thirds of the Run 3 LHCb RICH photon detector area. A best-value for the SPTR of the MAPMT read out by the electronic readout chain is extracted with respect to the MCP-PMT reference time. This is achieved by subdividing the data set in MCP-PMT reference TDC bins and in MAPMT channel ToT bins followed by a weighted recombination of the result.

5.1 Recorded data

5.1.1 Beam test data

Runs were recorded at the SPS beam facility in three configurations for the 1-inch MAPMT, using the working points described in section 4. These runs are concatenated into data sets with the following statistics:

- Focused Cherenkov ring and −900 V bias, about 8 million events
- Focused Cherenkov ring and −1000 V bias, about 2 million events
- Defocused Cherenkov ring and −1000 V bias, about 6 million events

The corresponding hit maps on half of the MAPMT surface (4×8 channels) are displayed in figure 21. These hit maps are in the perspective of the beam coming at the viewer, which is the opposite of the photograph in figure 10. In the defocused configuration, the distance between the lens and the photocathode plane is increased by approximately 10 mm. This results in a larger ring radius, which is compensated by translating the photon detectors away from the beam line, and a wider ring thickness, which is intended to increase the number of illuminated channels. The distribution of the number of hits per event is shown in figure 22 (left), with typically three hits per event in the MAPMT. Events containing more than 10 hits were removed from the hit maps and the analysis. These hits are generally more diffused across the MAPMT area and caused by multiple tracks simultaneously passing through

2025 JINST 20 P03034

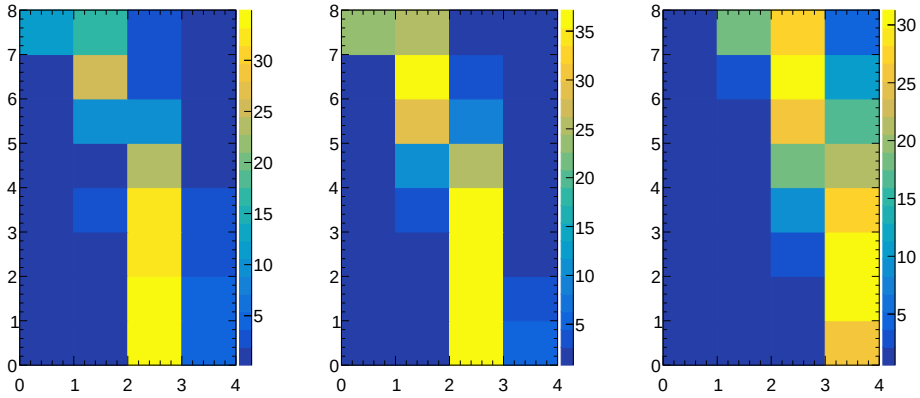

Figure 21. MAPMT hit maps for the focused-ring configuration at −900 V (left) and at −1000 V (centre) bias, as well as the defocused-ring configuation at −1000 V (right). The colour scale indicates the fraction [%] of hits per event for each channel.

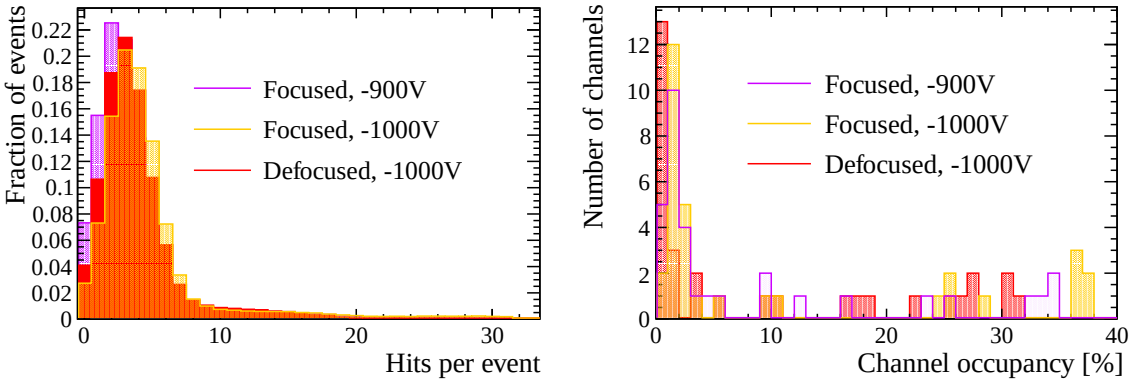

Figure 22. Left: number of hits per event in the 1-inch MAPMT for the three main data-taking conditions at the SPS beam test. Right: average channel occupancy for the 32 channels of the 1-inch MAPMT at the SPS beam test.

the RICH setup following a beam interaction with material placed upstream in the experimental area. The channel occupancy in figure 22 (right) shows two distributions, related to channels on the Cherenkov ring (occupancy ≥ 20 %) and channels outside the ring (occupancy < 20 %). The timing results will be presented only for channels on the Cherenkov ring, which have better statistics and correlation with the particle tracks.

5.1.2 Pulsed laser data

A reference study on the 1-inch MAPMT, at −1000 V bias, coupled to the electronic readout chain was performed using the pulsed-laser setup, recording data sets with ten million events each. Single-photon occupancies of 2 ± 1 %, 10 ± 5 % and 20 ± 10 % were achieved using neutral-density filters of 3.00, 2.70 and 2.30 in front of the MAPMT. The hit maps for the three configurations are displayed in figure 23. The distributions for the number of hits per event and the average channel occupancy are shown in figure 24.

2025 JINST 20 P03034

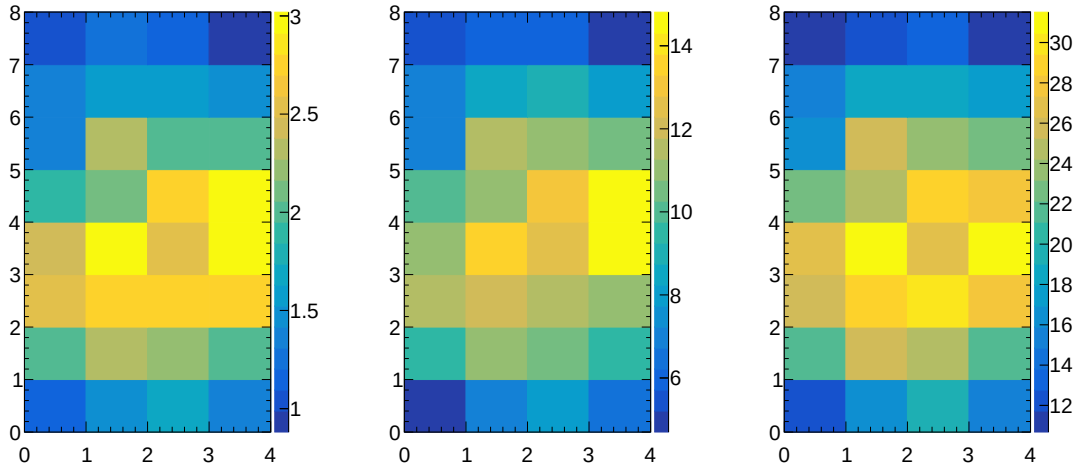

Figure 23. MAPMT hit map obtained with the picosecond pulsed laser setup in condition of peak occupancy approximately 2%, 10%, 20%. The occupancy is defined as the percentage of trigger events for which the channel registers a hit.

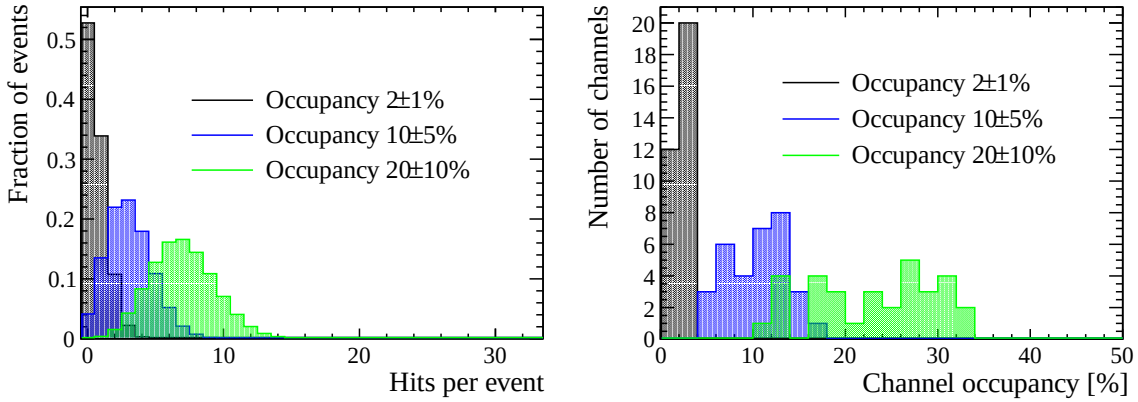

Figure 24. Left: number of hits per event in the 1-inch MAPMT for the three photon occupancy conditions at the laser tests. Right: average channel occupancy for the 32 channels of the 1-inch MAPMT at the laser tests.

5.2 SPTR with respect to the MCP-PMT reference

In this analysis [17], the data are subdivided in order to remove two main contributions to the time resolution: (a) time-walk and (b) TDC-bin variation. Time walk (a) arises from the variation in MAPMT signal amplitudes, which at a fixed threshold leads to earlier ToA for large signals and later ToA for signals close to the threshold. This effect can be decoupled from the SPTR by dividing the data into one subset per ToT bin. The time-walk within a ToT bin is negligible as the signals have approximately the same pulse shape. The variation in TDC bin width (b), as described in section 2.3.2, is present in both the MCP-PMT reference time and the MAPMT channel under study. In order to group events with equal TDC uncertainty in the reference time, and optimally account for this uncertainty, the data are subdivided with respect to the MCP-PMT ToA bin. In practice, the slow clock period of the TDC-core described in section 2.3 covers 16 TDC bins, after which the pattern of

2025 JINST 20 P03034

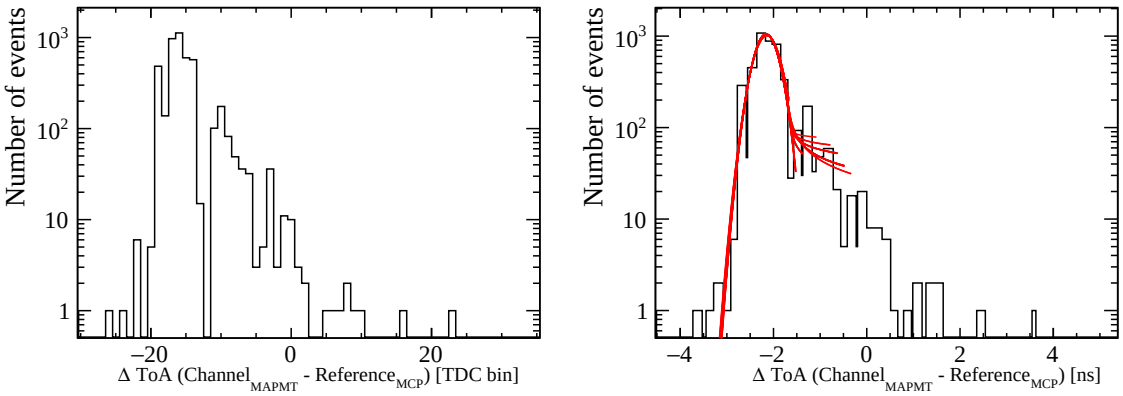

Figure 25. Left: the time difference distribution of a 1-inch MAPMT with respect to the MCP-PMT, in units of TDC bins. These data are a subset for one MCP-PMT ToA bin. Right: the same distribution as left, using the calibration data to convert to nanoseconds for the MAPMT TDC bins and the single MCP-PMT reference bin.

bin width variation is repeated. The data were therefore subdivided into 16 groups by accumulating these repeated bins (in total 14 sets of 16 repeated bins, spanning 32 ns).

The data for a single MCP-PMT TDC bin group are shown in figure 25 (left) in units of TDC bins. A pattern arises from the variable bin width of the TDC, where narrower TDC bins (on the MAPMT channel) are less populated with events than wider TDC bins. In figure 25 (right), this effect is corrected using the calibration data from section 2.3.2. The time of each bin was calculated using the sum of all the preceding bin widths plus half the width in picoseconds of the bin of interest. The histogram in figure 25 (right) uses variable bin widths reflecting the TDC bin width.

The time difference distributions are fitted using the CrystalBall function, where the time resolution is extracted as the Gaussian sigma parameter. Several fits are performed changing the fit range in order to account for parameter fluctuations. A subset of Gaussian sigmas is obtained selecting only the fits with parameters satisfying some minimum requirements to assess the good quality of the fit (mean within ±500 ps from the maximum of the distribution, σ within a range of 100 to 600 ps, uncertainties on σ below 50% of its value and a CrystalBall fit parameter $n > 10^{-4}$). The time resolution representative of this subset, $\hat{\sigma}_t^{\text{bin}}$, where bin denotes a previously described subset of a single MCP-PMT ToA bin, is obtained choosing the Gaussian sigma which is closest to the aforementioned mean, assigning as uncertainty the quadratic sum of the fit uncertainty and the standard deviation of the subset. For each MCP-PMT ToA bin, the time resolution is estimated by subtracting the MCP-PMT TDC bin width contribution:

$$\sigma_t^{\text{bin}} = \sqrt{(\hat{\sigma}_t^{\text{bin}})^2 - (\sigma_t^{\text{MCPbin}})^2} \tag{5.1}$$

Here, σ_t^{MCPbin} is obtained by dividing the MCP-PMT ToA bin width of the subset by $\sqrt{12}$. The uncertainty on σ_t^{bin}, which will be denoted $\sigma_{\sigma_t^{\text{bin}}}$, is extracted by combining, in quadrature, the statistical contribution coming from the fit uncertainty and the systematic contribution given by the standard deviation of the set of successful fits.

Starting from these fitted subsets, the time resolutions are recombined in the following two stages to obtain the SPTR.

2025 JINST 20 P03034

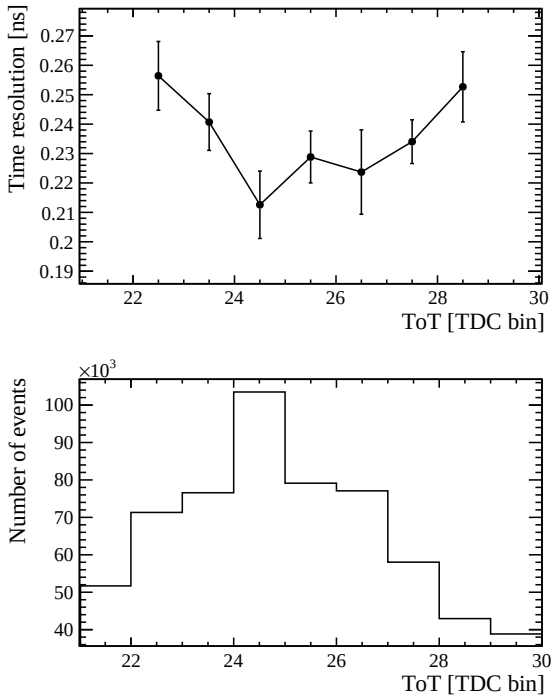

Figure 26. 1-inch MAPMT time resolution (after recombination this will correspond to σ_{meas} in Equation 5.5) with respect to the MCP-PMT reference time, plotted as a function of the MAPMT ToT in units of TDC bins.

- The 16 obtained values of σ_t^{bin} from the MCP-PMT ToA groups are recombined using a weighted average:

$$\sigma_{t,\text{singleToT}} = \frac{\sum_{\text{bin}=1}^{16} \sigma_t^{\text{bin}} / (\sigma_{\sigma_t^{\text{bin}}})^2}{\sum_{\text{bin}=1}^{16} 1/(\sigma_{\sigma_t^{\text{bin}}})^2} \tag{5.2}$$

  The results represent the time resolution for each subset of a single ToT bin, $\sigma_{t,\text{singleToT}}$.

  To account for uncertainty underestimations, the reduced χ^2 of each σ_t^{bin} with respect to the weighted average, $\sigma_{t,\text{singleToT}}$, is computed. If such reduced χ^2 is higher than 1, the uncertainty on σ_t^{bin} is weighted as follows [18]:

$$\chi_r^2 = \sum_{\text{bin}=1}^{16} \frac{(\sigma_t^{\text{bin}} - \sigma_{t,\text{singleToT}})^2}{\sigma^2_{\sigma_t^{\text{bin}}} \cdot (16-1)} \quad , \quad \sigma^{new}_{\sigma_t^{\text{bin}}} = \sqrt{\chi_r^2} \cdot \sigma_{\sigma_t^{\text{bin}}} \tag{5.3}$$

- In figure 26, the time resolution of a typical MAPMT channel with respect to the MCP-PMT is reported as a function of the MAPMT ToT bin number. A ToT range of ±3 bins around the most populated bin was chosen. In order to combine the time resolutions from these ToT bins, each $\sigma_{t,\text{singleToT}}$ was summed quadratically weighted by its statistics:

$$\sigma_t^2 = \frac{\sum_{\text{ToTbin}} N_{\text{ToT}} \cdot \sigma^2_{t,\text{singleToT}}}{\sum_{\text{ToTbin}} N_{\text{ToT}}} \tag{5.4}$$

2025 JINST 20 P03034

5.3 Summary of results

5.3.1 Corrections to the SPTR estimate

In order to extract the MAPMT channel time resolution (σ_{ch}), a correction needs to be made for the reference time and electronics time resolutions:

$$\sigma^2_{\text{meas}} = \sigma^2_{\text{ch}} + \sigma^2_{\text{tref}} + \sigma^2_{\text{TDC,ch}} + \sigma^2_{FastIC} \tag{5.5}$$

where

- σ_{meas} is the time resolution obtained from the analysis in section 5.2.
- σ_{ch} is the MAPMT sensor time resolution under study.
- σ_{tref} is the time resolution for the track reference. Using the MCP-PMT, $\sigma_{\text{tref}} \approx 100\,\text{ps}$ or using the pulsed laser, $\sigma_{\text{tref}} \approx 21\,\text{ps}$.
- $\sigma_{\text{TDC,ch}}$ is the TDC contribution estimated from the nominal TDC bin width, $\sigma_{\text{TDC,ch}} = 148.8/\sqrt{12}\,\text{ps}$. For the track reference time, the TDC contribution has already been corrected before the weighted recombination resulting in σ_{meas}.
- σ_{FastIC} is the jitter introduced by the FastIC of nominally $\sigma_{FastIC} \approx 25\,\text{ps}$.

5.3.2 SPTR results for beam test data

The time resolution results, σ_{ch}, of the 1-inch MAPMT at $-1000\,\text{V}$ bias for the beam test data are shown in table 1 and figure 27. For each data set, the hit occupancy cuts are applied to select only the channels on the Cherenkov ring. In the table, the average time resolution is computed as the mean with the uncertainty obtained from the standard deviation on the MAPMT channel time resolutions. A distinction was made between all channels on the ring and those excluding the edge channels in figure 27. The fraction of hits outside a window of $\pm 3\sigma_t$ is reported to quantify the tail of the distribution as shown in figure 25.

Table 1. Average time resolution over the MAPMT channels on the Cherenkov ring with respect to the MCP-PMT. The column 'excl. edge' omits the edge channels on the sensor which were observed to have a worse time resolution.

Geometry	Bias voltage [V]	σ_{ch} [ps]	σ_t [ps] (excl. edge)	Events > 3σ [%]
Focused	−1000	217 ± 71	182 ± 24	9.9
Defocused	−1000	239 ± 83	214 ± 21	8.3
Focused	−900	234 ± 36	222 ± 28	10.1

5.3.3 SPTR results for pulsed-laser data

The results for the 1-inch MAPMT time resolution, σ_{ch}, for the laser data set are shown in table 2 and figure 28. The tabulated time resolution is computed as the mean of all 32 channels with the uncertainty obtained from the standard deviation of the data set. Three different average photon occupancies (the fraction of events with a single-photon signal) are presented, where the uncertainty represents the minimum and maximum average occupancies on the sensor due to non-uniform illumination of the laser light spot in figure 23.

2025 JINST 20 P03034

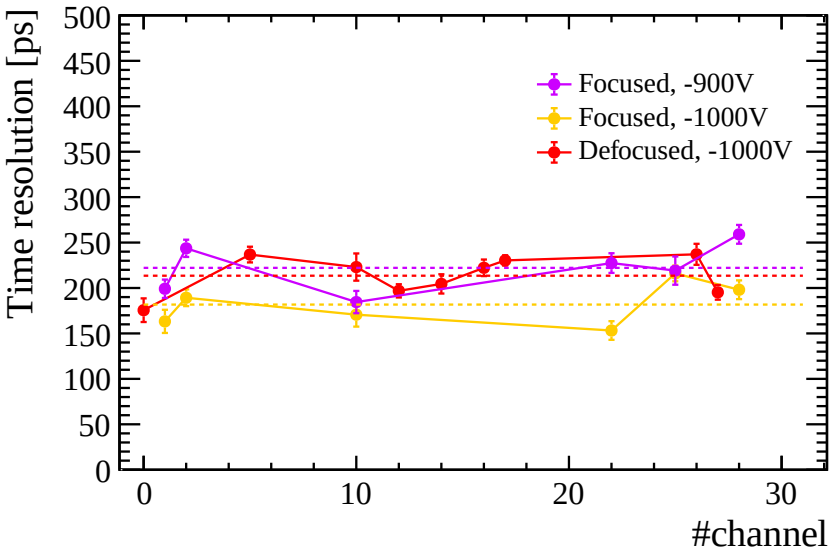

Figure 27. Time resolution (σ_{ch}) as a function of the MAPMT channel on the Cherenkov ring.

Table 2. Average time resolution results for the laser data sets using the synchronous laser output as the reference time.

Photon Occupancy [%]	Illuminated channels	σ_t [ps]
2 ± 1	All	162 ± 19
10 ± 5	All	178 ± 27
	Single channel (mask)	173 ± 25
20 ± 10	All	202 ± 24
	Single channel (mask)	170 ± 24

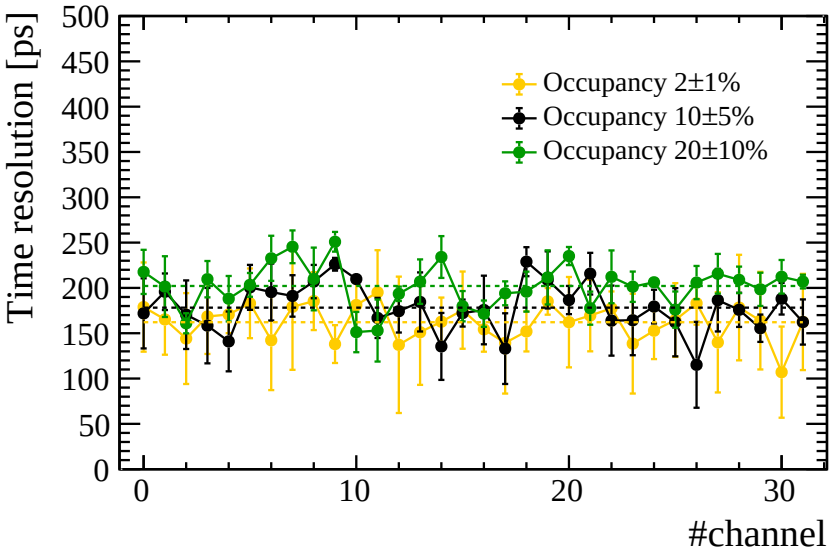

Figure 28. Laser data for the 1-inch MAPMT at −1000 V bias, showing the time resolution as a function of the channel number.

5.3.4 Discussion of the results

The SPTR results are generally consistent within uncertainty with the nominal TTS value of the 1-inch MAPMT of about 150 ps [19]. For the RICH upgrades R&D programme, this is an important step and the first demonstration of the sub-nanosecond timing performance of a full prototype optoelectronic readout chain. The contribution from the FastIC front-end ASIC to the overall time resolution is negligible compared to the TTS.

A good agreement between beam test and laser data was observed, with 182 ± 24 ps during beam test and 202 ± 24 ps during the laser tests at 20 ± 10 % occupancy and all channels illuminated. While this photon occupancy most closely represents the beam test conditions, the shape of the illuminated region is different, with a focused ring in the beam test and a diffuse spot from the mono-mode laser fibre and optics. The increased hit rate at higher occupancy is expected to lead to more electronic switching noise from the CMOS outputs on the FastICs as well as increased cross-talk. This may lead to a degradation in time resolution as observed in table 2, from 162 ± 19 ps at 2 % to 202 ± 24 ps at 20 %. The application of a mask to remove all hits (and hit-related switching noise) except for the channel of interest, recovers the time resolution to 170 ± 24 ps at 20 %. This effect may also play a role in the degradation of the time resolution from the focused (182 ± 24 ps) to the defocused (214 ± 21 ps) configuration, where more channels are illuminated. However, the different subset of illuminated pixels may also have increased the obtained average time resolution as shown in figure 21. The agreement between beam test and pulsed-laser results confirms that the time-resolution of the MCP-PMT track reference time was well estimated from the comparison against the other track reference detectors (section 3.3).

As expected, the time resolution degrades (from 182 ± 24 ps to 222 ± 28 ps) when the bias voltage is reduced from −1000 V to −900 V. More detailed studies of the dependency of TTS on bias voltage are foreseen. The worsening of time resolution for a few channels on the edge of the MAPMT during beam test was not confirmed by the pulsed-laser lab measurements, and will also be subject to further studies. A difference between central and edge channels on the MAPMT could arise from the bias voltage wire grid that focuses photoelectrons from the cathode to the first dynode. This grid has a different structure for edge channels. Since the illumination pattern was different for the beam test and laser studies, a follow up study will be performed comparing the time resolution at different positions using a more systematic illumination. The tail of the distribution, as quantified in table 1, is expected to be attributed to the same effect where a fraction of the photoelectrons arrives at a later time due to the non-uniform electric field generated by the focusing wire grid.

6 Multi-track correlation studies

A study of the synchronisation between the telescope (section 3.3) and the RICH system has been performed with the aim of finding a correlation between multi-track events and the number of hits in the 1-inch MAPMT. This is an important study to understand the synchronicity between sub-detectors during the beam test. It provides the first step towards synchronised running where the beam multiplicity information can be used to interpret events and to resolve, using the RICH hit times in data, tracks that arrive about 1 ns apart (or less), which is the ultimate goal for the use of time information in the LHCb experiment. Given the measured beam rate (approximately 100 kHz)

2025 JINST 20 P03034

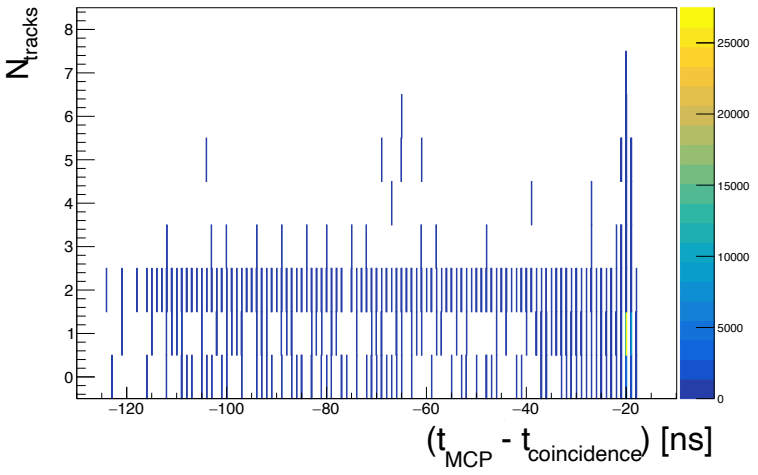

Figure 29. Number of reconstructed tracks in a ±100 ns time interval around the RICH coincidence time against the time difference between the RICH MCP and coincidence signals.

and the RICH readout interval of 32 ns, only one-track and two-track events are considered, since the fraction of events with more than two tracks is negligible.

In the telescope data, the 'local' synchronisation was first checked between (a) the picoTDC timestamp of the RICH coincidence and RICH MCP-PMT signal and (b) the measured particle track timestamp. This check is performed by looking at the number of tracks in a specific time interval around $\Delta T_{\text{MCP-coin}} = t_{\text{MCP}} - t_{\text{coincidence}}$. In the RICH coincidence, the MCP-PMT signal is intentionally delayed by about 20 ns with respect to the scintillator signals, in order to improve the trigger time resolution: for a typical one-track event the trigger time is driven by the delayed MCP-PMT signal. This results in an offset of $\Delta T_{\text{MCP-coin}} = -20$ ns. In case of two-track events, there could be an anticipated MCP-PMT signal without the corresponding scintillator signal (e.g. a peripheral particle detected by the 1-inch MCP-PMT channel but outside the spatial acceptance of the scintillators). Here, if the MCP-PMT time in the coincidence precedes the scintillator time and the coincidence time is driven by scintillators, $\Delta T_{\text{MCP-coin}} < -20$ ns, for which a two-track event is expected in the telescope data. This correlation is shown in figure 29 with the number of reconstructed tracks in a time interval ±100 ns around the RICH coincidence as a function of $\Delta T_{\text{MCP-coin}}$. Here, the bulk of one-track events is seen at −20 ns and the pileup tail below −20 ns is dominated by two-track events as expected.

At the next stage, event-by-event synchronisation between the RICH and telescope data is studied. To improve the synchronisation between the two systems, a signature reference signal, consisting of a pulse at precisely 400 ns from the last signal, is sent to the telescope after every 128 RICH coincidences. However, event synchronisation was generally not observed due to several challenges:

- The RICH trigger time is given by the coincidence time (of signals *A* and *B* in figure 14) synchronised to the internal clock of the trigger-logic unit. This resulted in a misalignment between the RICH readout window (defined by the trigger time) and the external track reference time (defined by the coincidence time). Hence, hits from the second track of multi-track events could be outside the RICH readout window.

- A majority of the combined runs have low track reconstruction efficiency and few events with multiple reconstructed tracks.

2025 JINST 20 P03034

- The number of pixels in the acceptance is limited (8-9 for 1-inch MAPMT) resulting in 3-4 hits per track. Moreover, in a two-track event, photons originating from the Cherenkov ring of the second track could illuminate the pixels that already have hits from the first track. This effect results in a small difference (1-2 hits on average) between the number of hits for one-track and two-track events which cannot be distinguished from statistical fluctuations in a single event.

- There can be RICH event losses (one or more RICH coincidence signals are not registered by the picoTDC and the synchronisation is shifted by the number of lost events) and the addition of spurious picoTDC events (the synchronisation is shifted in the opposite direction by the number of spurious events). The spurious picoTDC events can be: (i) events with $dt[i]$ less than the RICH trigger dead time of 500 ns, (ii) events with $dt[i]$ less than the RICH trigger dead time arriving immediately after a reference signal.

Nevertheless, a global synchronisation was searched for after the removal of spurious picoTDC events, with the aim of finding a set of RICH coincidence events where the mean number of hits in the 1-inch MAPMTs is significantly larger for two-track than for one-track events. To increase the number of two-track events, the run with the highest track reconstruction efficiency (about 84%) is chosen. The time interval for the track reconstruction is reduced to ±20 ns around the reference time to better match the 32 ns RICH readout window, and events with $\Delta T_{\text{MCP-coin}}$ around −20 ns are selected.

A scan of the whole run, containing n events, is performed using a fixed number of $m < n$ events and stepping the m-events starting point ('left border' in figure 30) in the run. For each interval the mean number of hits in the MAPMTs is obtained from a Poisson fit of the number of hits for one-track events and two-tracks events. A significant increase of the ratio $\bar{N}_{\text{hits}}(2\text{ tracks})/\bar{N}_{\text{hits}}(1\text{ track})$ would be an indication of synchronisation in the corresponding m-events interval.

The procedure is repeated by shifting RICH events with respect to telescope picoTDC events during the event matching. Since a small number of event losses was typically observed, introducing this shift may resynchronise the run. As shown in figure 30 (right), a shift in the range from −5 to +5 was chosen (where shift= 0 corresponds to non-shifted events) for the optimised number of $m = 16000$ RICH coincidence events in the interval. The best synchronisation is observed for a

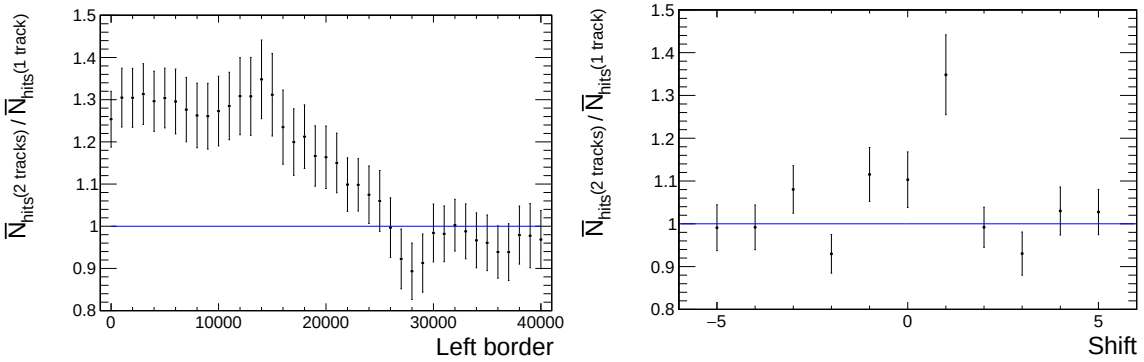

Figure 30. Left: ratio of the mean number of hits for two-track events to the mean number of hits for one-track events as a function of the left border of an interval of 16000 RICH coincidence events. Right: ratio of the mean number of hits for two-track events to the mean number of hits for one-track events as a function of the applied shift during the matching of telescope and RICH events. Blue line: the ratio value corresponding to an equal mean number of hits for one-track events and two-track events.

2025 JINST 20 P03034

shift of +1, which corresponds to a synchronisation in approximately the first half of the run and indicates the loss of a RICH event at the beginning of the run. Here, the maximum ratio corresponds to the left border equal to 14000, or to the range [14000, 30000]. The ratio as a function of the shift for this [14000, 30000] interval is shown in figure 30 (right). The significance of the increases in figure 30 (right) with respect to the hypothesis of no increase ($\bar{N}_{\text{hits}}(2 \text{ tracks})/\bar{N}_{\text{hits}}(1 \text{ track}) = 1$) has been estimated with a toy MC. A 5 σ significance has been obtained for the ratio value corresponding to shift of +1, while the ratio values for the other shifts have a significance <2 σ and are compatible with fluctuations due to limited statistics of two-track events in the selected interval.

7 Conclusion

A novel optoelectronic readout chain was operated at the SPS charged particle beam facility. Single-photons on a Cherenkov ring were successfully detected using MAPMT and SiPM sensors. The FastIC (nominal time resolution of 25 ps) output signals were timestamped using a custom-developed TDC-in-FPGA with calibrated time bin width of 150 ps on average. A track reference timestamp in data was provided using an MCP-PMT on the beam line ($\sigma \approx 100$ ps). The correlation between events in the RICH detector setup and the track telescope was investigated and an increased photon yield in the RICH detectors was observed for a subset of the data. The FastIC ASIC configuration and threshold working point were carefully analysed using a pulsed-laser setup in the lab, with the aim of finding the optimal relative photon detection efficiency and time resolution.

A detailed analysis was performed on the SPTR of the 32 channels read out for the 1-inch MAPMT. The analysis corrects for time-walk, TDC-in-FPGA bin width variations and the MCP-PMT reference time resolutions. At −1000 V bias voltage, the optimal SPTR for channels on the Cherenkov ring and in the centre of the MAPMT was found to be 182 ± 24 ps, which is consistent with the approximately 150 ps time resolution from reference measurements. These studies demonstrate the first sub-nanosecond timing measurement for the LHCb RICH beam test campaign and set an important precedence for further studies towards the upgrade of the RICH detectors for high pile-up conditions at the HL-LHC. Given the complexity of the new equipment and the first sub-nanosecond timing measurements, as well as the effort to thoroughly understand the detailed signal shape, noise behaviour and time-resolution of the new optoelectronics chain, the scope of this paper was limited to the evaluation of the time-resolution of the 1-inch MAPMT. This study took precedence as the 1-inch MAPMT will remain the photon sensor during Run 4 with the picosecond timing readout electronics installed at the LS3 Enhancements. Future beam tests will also be dedicated to the assessment of the time resolution capabilities of the SiPMs and the 2-inch MAPMT. The successful detection of Cherenkov photons performed with these sensors during the beam test campaign provides an excellent starting point for these future studies.

The optoelectronic readout chain will be further developed to introduce an ASIC-only solution and to remove several of the limitations (in time resolution, channel density and stability of operation) of the prototype. Ultimately, the novel FastRICH ASIC will be integrated and tested for the LHCb LS3 Enhancement programme.

Acknowledgments

The beam test campaign has been performed in the framework of the LHCb RICH Experiment. Some of the developments presented in this contribution are performed in collaboration with the CERN EP R&D

2025 JINST 20 P03034

programme on technologies for future experiments. This project has received funding from the European Union's Horizon Europe Research and Innovation programme under Grant Agreement No 101057511, and from Institute of Atomic Physics Bucharest (IFA) through LHCb-RO grant number 5/03.01.2022.

The authors wish to express their gratitude towards the FastIC Collaboration for the ASIC support. Our gratitude extends to the TimePix4 Collaboration and in particular Tommaso Pajero for contributing figure 16.

References

[1] F. Keizer, *Sub-nanosecond Cherenkov photon detection for LHCb particle identification in high-occupancy conditions and semiconductor tracking for muon scattering tomography*, Ph.D. thesis, Cambridge University, Cambridge University, U.K. (2020) [CERN-THESIS-2019-203].

[2] LHCb collaboration, *The LHCb Upgrade I*, 2024 *JINST* **19** P05065 [arXiv:2305.10515].

[3] M. Baszczyk et al., *CLARO: an ASIC for high rate single photon counting with multi-anode photomultipliers*, 2017 *JINST* **12** P08019.

[4] R. Lindner, *LHCb Particle Identification Enhancement Technical Design Report*, CERN-LHCC-2023-005, CERN, Geneva (2023) [DOI:10.17181/CERN.LAZM.F5OH].

[5] FastRICH collaboration, *FastRICH ASIC Documentation*, https://fastrich.docs.cern.ch.

[6] F. Keizer, *The FastRICH ASIC for the LHCb RICH enhancements*, *Nucl. Instrum. Meth. A* **1067** (2024) 169664.

[7] LHCb collaboration, *Framework TDR for the LHCb Upgrade II: Opportunities in flavour physics, and beyond, in the HL-LHC era*, CERN-LHCC-2021-012, CERN, Geneva (2021) [DOI:10.17181/CERN.NTVH.Q21W].

[8] S. Gómez et al., *FastIC: a fast integrated circuit for the readout of high performance detectors*, 2022 *JINST* **17** C05027.

[9] L. Cojocariu, D. Foulds-Holt, F. Keizer, V. Placinta and S. Wotton, *A multi-channel TDC-in-FPGA with 150 ps bins for time-resolved readout of Cherenkov photons*, *Nucl. Instrum. Meth. A* **1055** (2023) 168483.

[10] Y. Wang, P. Kuang and C. Liu, *A 256-channel multi-phase clock sampling-based time-to-digital converter implemented in a Kintex-7 FPGA*, in the proceedings of the *IEEE International Instrumentation and Measurement Technology Conference*, Taipei, Taiwan, May 23–26 (2016) [DOI:10.1109/i2mtc.2016.7520401].

[11] L. Cadamuro et al., *Characterization of the Hamamatsu R11265-103-M64 multi-anode photomultiplier tube*, 2014 *JINST* **9** P06021 [arXiv:1403.3215].

[12] M. Calvi et al., *Characterization of the Hamamatsu H12700A-03 and R12699-03 multi-anode photomultiplier tubes*, 2015 *JINST* **10** P09021 [arXiv:1506.04302].

[13] R. Cardinale et al., *Development of an integrated housing for Silicon Photomultipliers for future Ring Imaging Cherenkov photo-detectors*, *Nucl. Instrum. Meth. A* **1055** (2023) 168476.

[14] M.K. Baszczyk et al., *Test of the photon detection system for the LHCb RICH Upgrade in a charged particle beam*, 2017 *JINST* **12** P01012 [arXiv:1610.02879].

[15] K. Akiba et al., *Reconstruction of charged tracks with Timepix4 ASICs*, 2023 *JINST* **18** P02011 [arXiv:2210.01442].

[16] S. Altruda et al., *PicoTDC: a flexible 64 channel TDC with picosecond resolution*, 2023 *JINST* **18** P07012.

[17] F. Borgato, *The road to a time-resolved RICH at LHCb*, *PoS* **EPS-HEP2023** (2024) 563.

[18] Particle Data Group collaboration, *Review of Particle Physics*, *PTEP* **2022** (2022) 083C01.

[19] M. Calvi et al., *Single photon time resolution of photodetectors at high rate: Hamamatsu R13742 MaPMT and R10754 MCP-PMT*, 2020 *JINST* **15** P10031 [arXiv:2007.08937].

2025 JINST 20 P03034